RSC Advances

ROYAL SOCIETY OF CHEMISTRY

www.rsc.org/advances

Graphical Abstract

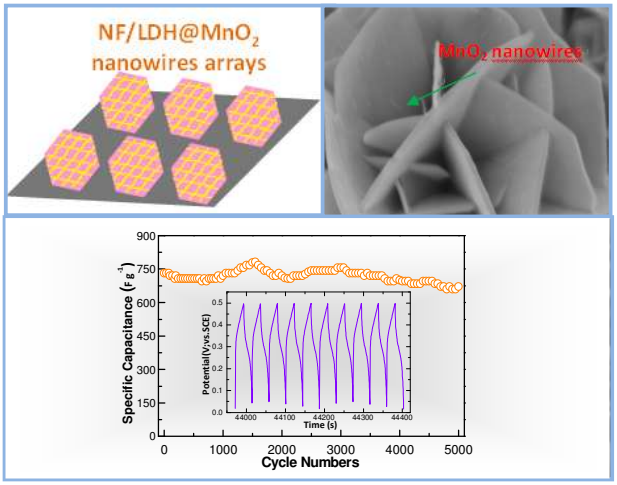

Engineering One-Dimensional and Two-Dimensional Birnessite Manganese Dioxides on Nickel Foam-Supported Cobalt-Aluminum Layered Double Hydroxides for Advanced Binder-Free Supercapacitors

Xiaodong Hao[a], *Yuxin Zhang*[a,b,*], *Zengpeng Diao*[a], *Houwen Chen*[a,*], *Aiping Zhang*[a], *Zhongchang Wang*[c,*]

[a]College of Material Science and Engineering, Chongqing University, Chongqing 400044, P.R. China

[b]National Key Laboratory of Fundamental Science of Micro/Nano-Devices and System Technology, Chongqing University, Chongqing 400044, P.R. China

[c]Advanced Institute for Materials Research, Tohoku University, 2-1-1, Katahira, Aoba-ku, Sendai 980-8577, Japan

* Corresponding author. Tel.: +86 23 65104131;

Fax: +86 23 65104131

E-mail: zhangyuxin@cqu.edu.cn (Y.Z.); hwchen@cqu.edu.cn (H.C.); zcwang@wpi-aimr.tohoku.ac.jp (Z.W.)

Abstract

We report a facile decoration of the hierarchical nickel foam-supported CoAl layered double hydroxides (CoAl LDHs) with MnO_2 nanowires and nanosheets by a chemical bath method and a hydrothermal approach for the high-performance supercapacitors. We demonstrate that owing to the sophisticated configuration of binder-free LDH@MnO_2 on the conductive Ni foam (NF), the designed NF/LDH@MnO_2 nanowires composites exhibit a highly boosted specific capacitance of 1837.8 Fg^{-1} at a current density of 1 Ag^{-1}, a good rate capability, and an excellent cycling stability (91.8% retention after 5000 cycles). By applying the hierarchical NF/LDH@MnO_2 nanowires as the positive electrode and activated microwave exfoliated graphite oxide activated graphene as the negative electrode, the fabricated asymmetric supercapacitor produces an energy density of 34.2 $Whkg^{-1}$ with a maximum power density of 9 $kWkg^{-1}$. Such strategies with controllable assembly capability could open up a new and facile avenue in fabricating advanced binder-free energy storage electrodes.

***Keywords*:** Energy storage; Layered double hydroxides; Manganese dioxide; Supercapacitors

Introduction

With sharp increasing demand on energy storage for electric vehicles and mobile electronics, supercapacitors with desirable functionalities of fast charging (within seconds), high power density (ten times more power than batteries) and excellent cycling stability (over 1000 cycles) have become one of the most promising candidates for next-generation energy storage devices.[1, 2] In light of the charge storage mechanism, supercapacitors can in general be classified into electrical double layer capacitors (EDLCs) and pseudocapacitors. Pseudocapacitors are desirable for performance enhancement,[3, 4] since their multiple oxidation states/structures enable the rich redox reactions for pseudocapacitance generation. Traditional pseudocapacitive materials mainly include typical transitional metal oxides/hydroxides, such as RuO_2, MnO_2, NiO, $Ni(OH)_2$, Co_3O_4, $Co(OH)_2$, Fe_3O_4, and their binary systems.[5-10] Among them, MnO_2 has been extensively applied due to their intriguing electrochemical properties involving high capacitance, low cost and environment-friendly nature.[11-15] However, there are two main drawbacks for MnO_2 as supercapacitors: (i) its poor conductivity (10^{-5}–10^{-6} S cm^{-1}), which limits the charge–discharge rate for high power applications[16, 17] and (ii) the low loading of active materials, which would lead to a low energy density (e.g. electrochemical deposition). Owing to these disadvantages, it remains a great challenge to promote electrochemical utilization of pseudocapacitance of MnO_2 by designing MnO_2-based electrodes with novel structures and reliable electric connection alone.[18]

Very recently, an attractive concept emerges, allowing a direct growth of smart integrated array architectures onto conducting substrates as binder-free electrodes for supercapacitors via the combination of multi-component structures. This method provides synergistic effects from all of their individual constituents, thus achieving high power and energy density, long cycle life, and high rate capability. Since it is generally believed that an ideal electrode material consists of a three-dimensional (3D) interpenetrating network of electron and ion pathways for efficient mass/electron transportation,[19-21] a key challenge is to develop a desirable electrode architecture that favors sufficient exposure of electroactive species for Faradaic redox reaction, while enhancing kinetics of ion/electron transport throughout the electrode. In view of these considerations, one promising route in obtaining the highly-accessible surface area, fast ion diffusion and excellent electronic conductivity is through a

rational design by hybridizing pseudocapacitive oxides/hydroxides with sophisticated nanoarchitectures. For example, zhao *et al.* reported MnO_2 nanowires/CoAl-LDH/carbon fibers hierarchical nanocpmposites for high-performance supercapacitor (944 Fg^{-1} at 1 A g^{-1}).[18] It suggested that this kind of hierarchical nanocpmposites presented a promising future for the application of supercapacitor.

Here, we demonstrate the design and fabrication of a novel nanocomposite (MnO_2/LDH/NFs) by loading 1D and 2D MnO_2 onto CoAl layered double hydroxide (LDH) nanowalls which are grown on nickel foam (NF) as a binder-free electrode for the high-performance supercapacitors. By virtue of the synergetic contribution from the individual constituents and the sophisticated configuration, the resulting NF/LDH@MnO_2 nanowires composites exhibit a greatly enhanced specific capacitance of 1837.8 Fg^{-1} (1 Ag^{-1}), which is superior to its single-component sample (NF/LDH or NF/LDH@MnO_2 nanosheets). Unexpectedly, the integrated electrodes manifest an excellent long-term cycling stability (91.8% retention after 5000 cycles). Moreover, we also manufacture an asymmetric supercapacitor by applying the hierarchical NF/LDH@MnO_2 nanowires as positive electrode and the activated microwave exfoliated graphite oxide (aMEGO) as negative electrode, which exhibits an energy density of 34.2 $Whkg^{-1}$ with a maximum power density of 9 $kWkg^{-1}$.

Experimental

All chemical reagents were of analytical purity and used with no further purification. The CoAl-LDH arrays on nickel foam (NF) were synthesized by a modified hydrothermal method.[22] The $Co(NO_3)_2 \cdot 6H_2O$ (0.01 M), $Al(NO_3)_3 \cdot 9H_2O$ (0.005 M), NH_4F (0.05 M) and urea (0.35 M) were dissolved with the aid of ultra-sonication to obtain a homogeneous solution (40 mL). The Ni foam (2*3 cm^2) was carefully cleaned with diluted HCl solution to remove the NiO layers on the surface, followed by a further cleaning with deionized water and ethanol. The aqueous solution and the Ni foam were transferred into a Teflon-lined stainless steel autoclave and maintained at 120°C for 20 h, and then cooled down to room temperature. The samples were next rinsed several times with deionized water and ethanol, and dried at 60°C overnight.

The hierarchical NF/LDH@MnO_2 nanowires were prepared via a facile chemical bath method. The NF/LDH sample was immersed in 40 mL $KMnO_4$ solution (0.02 M), which was subsequently maintained at 30°C for 4 h. Finally, the samples were

removed, washed with deionized water and ethanol, and dried at 60°C, harvesting the hierarchical NF/LDH@MnO_2 nanowires. On the other hand, the hierarchical NF/LDH@MnO_2 nanosheets were prepared via a facile hydrothermal method. The NF/LDH sample was first introduced into a Teflon-line stainless steel autoclave containing 40 mL $KMnO_4$ solution (0.02 M), which was subsequently maintained at 140°C for 24 h. As above the samples were finally removed, washed with deionized water and ethanol, and dried at 60°C to obtain hierarchical NF/LDH@MnO_2 nanosheets.

The crystallographic information and chemical composition of the as-prepared products were obtained by the X-ray diffraction (XRD, D/max 1200, Cu K_α). Structure and morphology of the NF/LDH and NF/LDH@MnO_2 nanocomposites were investigated with focused ion beam (ZEISS AURIGA FIB/SEM) and transmission electron microscopy (TEM, ZEISS LIBRA 200). A three-electrode system was adopted to measure the response of the NF/LDH and NF/LDH@MnO_2 nanocomposites as the working electrodes. The 1 M LiOH aqueous solution was adopted as the electrolyte, and the platinum plate and the saturated calomel electrode (SCE) were used as counter and reference electrode, respectively. The Ni-foam-supported nanostructures (1 × 1 cm^2) were used directly as the working electrode. The asymmetric supercapacitor was measured with a two-electrode system, including two slices of electrode materials with the same size. A filter paper was used as separator, and 1 M LiOH solution as the electrolyte. In the two-electrode system, the hierarchical NF/LDH@MnO_2 nanowires arrays were adopted as a positive electrode. The negative electrode was produced by mixing activated microwave exfoliated graphite oxide, activated graphene (MEGO) and 10 wt% acetylene black and 10 wt% polyvinylidene fluoride (PVDF) in N-methyl-2-pyrrolidone (NMP) to form a paste, which was then pressed into uniform sheet.

The cyclic voltammetry (CV) and galvanostatic charge discharge techniques were employed to investigate electrochemical performance of the electrodes, which was measured using a CHI 660E electrochemical station. All the operating current densities were calculated based on the mass of active materials (mass of LDH@MnO_2 for three-electrode system and the total weight of LDH@MnO_2 with MEGO for two-electrode system). The electrochemical impedance spectroscopy (EIS) was conducted in a frequency range from 100 kHz to 0.01 Hz with a perturbation amplitude of 5 mV versus the open-circuit potential.

Results and discussion

Structure and morphology

Fig. 1 shows the XRD spectra of the NF/LDH and NF/LDH@MnO_2 nanocomposites. The four low-angle diffraction peaks can be indexed as (003), (006), (012) and (015) reflections of LDH phase (JCPDS 51-0045; Fig. 1A).[23] The weak peak at ~12.5^o (Fig. 1B; NF/LDH@MnO_2 nanosheets) can be indexed as (001) diffraction of the birnessite-type MnO_2 (JCPDS 80-1098), indicating that the birnessite-type MnO_2 can be formed during the hydrothermal reaction, consistent with the previous reports.[4, 14, 24] However, this peak is absent at the pattern of NF/LDH@MnO_2 nanowires due to low content of MnO_2.

Fig. 2A illustrates the fabrication route of hierarchical NF/LDH@MnO_2 nanocomposites. By virtue of the activation of substrates by the NH_4F, LDH arrays are grown on the Ni foam by a facile co-precipitation method under hydrothermal condition.[25] The smooth surface of Ni foam is obtained by the pretreatment of HCl, which favors the growth of LDH array (See Supplementary Information, SI-1). The deposition of MnO_2 on the LDH arrays can subsequently be engineered by two different methods. One is to introduce the NF/LDH arrays with MnO_2 nanowires under chemical bath reaction at 30^{o}C for 4 h and the other is to fabricate the CoAl-LDH@MnO_2 nanosheets under the hydrothermal reaction at 140^{o}C for 24 h. It should be noted that neither the carbon coating nor the electrochemical deposition is required in the deposition of MnO_2 phase because the MnO_2 nanowires on the LDH can be produced via an in situ spontaneous redox reaction between the Co^{2+} species in the LDH and $KMnO_4$,[18] while the $KMnO_4$ can be self-decomposed during hydrothermal reaction, leading to further formation of MnO_2 nanosheets on NF/LDH arrays.

The vertically-aligned and cross-linked LDH nanowalls grown on the Ni foam can serve as a robust and conductive base for loading additional active materials (See SI-2). The corresponding X-ray energy dispersive spectroscopy (EDS) mapping spectra of Co, Al, O and Ni, which confirm the evenly dispersion of LDH nanowalls on the Ni foam. These LDH nanowalls are ~ 46.7 nm in thickness and ~1021 nm in height (See SI-3). Such a thin hexagonal morphology of a single LDH nanocrystal is also confirmed in TEM image. Further selected area electron diffraction (SAED) pattern exhibits hexagonally

arranged spots, and HRTEM image and the corresponding fast Fourier transformation (FFT) pattern verify high crystallinity of LDH nanowalls (See SI-4). Moreover, EDS spectrum reveals the presence of Co, Al and O element with a Co/Al molar ration of 2.05, in line with the feed intake ration (Co:Al=2:1). Fig. 2B and c show typical SEM images, where one can note that the deposition of MnO_2 nanowires onto hierarchical NF/LDH arrays can be controlled by simply immersing the NF/LDH samples into $KMnO_4$ aqueous solution at 30^oC for 4 h without stirring. The color of the NF turns brown (inset in Fig. 2B), in sharp contrast to the light pink of the NF/LDH (inset in SI-2b). However, the morphology of the LDH arrays does not alter at all by the deposition of MnO_2, which may be attributed to the mild condition under chemical bath reaction. The in situ redox reaction proceeds between Co^{2+} species within LDH and $KMnO_4$ in solution under mild conditions, leading to the formation of MnO_2 nanowires on the LDH host layers.[18] Fig. 2C shows the enlarged SEM image, revealing the presence of MnO_2 nanowires on the NF/LDH arrays. Fig. 2D and e shows the hierarchical NF/LDH@MnO_2 nanosheets arrays. Interestingly, the color of the NF turns dark (inset in Fig. 2D), indicating that $KMnO_4$ is self-decomposed to δ-MnO_2 nanosheets during the hydrothermal reaction. This may give rise to a full coverage of MnO_2 nanosheets on the LDH arrays. As seen in Fig. 2E, the NF/LDH arrays are carpeted with thin δ-MnO_2 nanosheets on both sides of LDH layers. Such universal distribution of the MnO_2 phase throughout the hierarchical structure for both NF/LDH@MnO_2 nanowires and NF/LDH@MnO_2 nanosheets arrays is confirmed by the EDS mapping (See SI-5). These resulting NF/LDH@MnO_2 heterostructures exhibit a fully integrated structure in which the NF provides a 3D backbone and the densely-packing LDH nanowalls serve as a support for the homogeneous distribution of the nanoscale MnO_2.

Fig. 3A and b presents the typical TEM images of the LDH@MnO_2 nanowires, in which numerous MnO_2 nanowires of ~1 nm in diameter are dispersed evenly on the LDH support, forming extra interconnected porosity. SAED analysis reveals the hexagonal diffraction, which is attributed to the {1010} crystalline planes of the LDH phase, indicating that LDH structure is retained on the immobile MnO_2 (inset in Fig.3A). No diffraction pattern related to MnO_2 is identified, suggesting an amorphous nature for the MnO_2 coating. These results are consistent with the XRD analysis. Further HRTEM and corresponding FFT pattern confirm that the introduction of MnO_2 nanowires does not damage the high crystallinity of the

LDH support. Fig. 3C and d presents the typical TEM images of LDH@MnO_2 nanosheets, from which LDH host layer is found to be densely decorated with numerous thin MnO_2 nanosheets. There appear three weak polycrystalline diffraction halos in the SEAD pattern (inset in Fig.3C), which are indexed to (200), (111), and (113) of δ-MnO_2 phase. HRTEM image reveals that part of MnO_2 nanosheets can grow epitaxially along LDH host layers (Fig. 3D). The measured lattice fringe distance is 0.212 nm, which matches that in the (-112) plane of δ-MnO_2, in line with the results of XRD data. In addition, STEM EDS mapping spectra of LDH@MnO_2 nanosheets confirm the epitaxial growth of MnO_2 nanosheets (See SI-6). The atomic ratio of Mn:Co element for NF/LDH@MnO_2 nanosheets and NF/LDH@MnO_2 nanowires (not showed) were 1:1.8 and 1:0.41, respectively. These data presented that only a few MnO_2 nanowires formed on the surface of LDH, while a densely MnO_2 nanosheets coating were fabricated during the hydrothermal reaction.

Electrochemical properties

The capacitive performance of the NF/LDH@MnO_2 nanowires composite is evaluated by the CV and the charge-discharge in the three-electrode systems. Fig. 4A shows CV curves of the NF/LDH@MnO_2 nanowires electrodes in 1 M LiOH aqueous electrolyte at a series of scan rates. Two pairs of redox peaks at ~0.2 and 0.55 V are clearly observed for the NF/LDH@MnO_2, which correspond to the reversible reaction of the Co^{2+}/Co^{3+} and Co^{3+}/Co^{4+} associated with OH^{-}[18]. The current response shows an increase trend with the rise of the scan rate, indicating a good capacitive behavior of the electrode. To further examine electrochemical performances of the NF/LDH@MnO_2 nanowires electrode, galvanostatic charge-discharge measurement is systematically performed on the NF/LDH@MnO_2 nanowires electrode at various currents (Fig. 4B). The discharge curves exhibit a typical pseudocapacitive behavior, in accordance with the CV results. The specific capacitance (Cs) of NF/LDH@MnO_2 nanowires electrode is estimated to be 1837.8 Fg^{-1} at a current density of 1 Ag^{-1}, indicating that NF/LDH@MnO_2 nanowires electrode has an excellent supercapacitor specific capacitance, even higher than those of CoAl-LDH based, MnO_2-based electrodes and hybrid pseudo-capacitive materials.[26-30] Compared to our previous report of LDH/MnO_2 nanocomposites, we find that Ni foam support not only serves as a great conductor, but imposes a stereoscopic geometry constraint on the growth of LDH nanowalls, which consequently give rise to formation of smaller and thinner LDH

nanowalls, thereby enhancing Li^+ penetration across the heterostructure.

We further investigate the relationship between specific capacitance and current density of NF/LDH@MnO_2 nanowires nanocomposite (Fig. 4C), and find that the specific capacitance decreases with the increase of the current density. The NF/LDH@MnO_2 nanowires electrode displays a moderate rate behavior with 44.3% of its initial capacitance maintaining when the current density increases to 10 Ag^{-1}. The capacitance retains a value of 220 Fg^{-1} even at a high current density of 50 Ag^{-1}. Fig. 4D presents the cycling life of the NF/LDH@MnO_2 nanowires electrode measured at 15 Ag^{-1}, the other important factor for supercapacitor application. Interestingly, the specific capacitance increases gradually (up to 6.8%) with the increasing of cycling number before the first 1500^{th} cycle, which might be due to the activation process during the cycling test.[31] During this process, the electrode is completely activated through the intercalation and de-intercalation of ions through some circulations, resulting in the increase of active points inside electrode materials and hence enhancing the specific capacitance. After 5000 cycles of charge and discharge process, the capacitance retains 91.8% of its original value, indicative of an excellent cycling stability. This is further verified by the stable charge-discharge curves in the last 10 cycles (inset in Fig. 4D).

The charge curves are still symmetric as compared to their corresponding discharge counterparts, indicating that the NF/LDH@MnO_2 nanowires electrode undergoes no obvious structural change during charge-discharge processes. The excellent cycling stability of the hierarchical NF/LDH@MnO_2 nanowires electrode can also be verified from the charge-discharge curves obtained at the current density of 1 Ag^{-1} before and after 5000 cycles (See SI-7). In this respect, the rational combination of the MnO_2 nanowires and LDH into a unique integrated architecture can substantially improve electrochemical properties. In the system of NF/LDH@MnO_2 nanowires structure, Ni foam serves as a porous substrate and a good current collector, which enables efficient charge transport of the composite. The as-grown LDH nanowalls for loading MnO_2 nanowires build a 3D macroporous framework with an electrolyte-filled network, enhancing ionic conductivity greatly and thereby ensuring a high utilization efficiency of the electrode material. The well distributed MnO_2 nanowires can thus form a hierarchical porous structure, which can minimize the solid-phase ion diffusion length.[18]

We also compare electrochemical performance of NF/LDH and NF/LDH@MnO_2 nanocomposites, as shown in Fig. 5. For the three CV curves measured at a scan rate of 20 mVs^{-1}, the enclosed area of NF/LDH@MnO_2 nanowires is broadest in comparison to those of NF/LDH and NF/LDH@MnO_2 nanosheets (Fig. 5A), suggesting that it has largest specific capacitance. Fig. 5B shows the discharge curves of the three electrodes within a potential range of 0-0.5V, from which the corresponding specific capacitance is estimated to be 1837.8, 1616, and 1377.8 Fg^{-1} at the current density of 1 Ag^{-1} for the NF/LDH@MnO_2 nanowires, NF/LDH@MnO_2 nanosheets and NF/LDH, respectively, thus confirming the highest specific capacitance for the NF/LDH@MnO_2 nanowires. Fig. 5C shows the specific capacitance of the three electrodes as a function of applied current density. Within the whole current density range, the NF/LDH@MnO_2 nanowires electrode yields a substantially higher specific capacitance than the other two samples. In particular, the gravimetric capacitance of NF/LDH@MnO_2 nanowires reaches 814 Fg^{-1} at a current density of 10 Ag^{-1}, higher than those of the NF/LDH@MnO_2 nanosheets (766 Fg^{-1}) and NF/LDH (458 Fg^{-1}) samples. The capacitance of NF/LDH decreases quickly as the charging-discharging rate increases from 1 to 30 Ag^{-1}, *i.e.* only 13.9 % of its original value is retained. In contrast, for the NF/LDH@MnO_2 nanowires and NF/LDH@MnO_2 nanosheets, 11.9% and 8.6% of their original capacitances are maintained even at a high current density of 50 Ag^{-1}, indicating that the introduction of MnO_2 into the system of NF/LDH can substantially improve its specific capacitance and rate capability.

In addition, we also conduct the cycling performance test over 1000 cycles for the three electrodes at 10 A g^{-1} using the galvanostatic charge-discharge technique in a potential window of 0-0.5 V (Fig. 5D). The NF/LDH electrode shares the increasing tendency as the NF/LDH@MnO_2 nanowires during the 1000-cycling test, while the NF/LDH@MnO_2 nanosheets electrode suffers a gradual decreasing with the retention of only 82.4% of its original capacitance. These results indicate that the decorated MnO_2 nanosheets film on the LDH support might capture the diffused ions during the cycling test, *i.e.* the amounts of intercalated and de-intercalated ions reduce, resulting in a continuous loss of its capacitance, albeit that the small and thin nanowires on the LDH support do not hinder the penetration of ions at all. Moreover, the Nyquist plots exhibit a nearly semicircle over the high frequency range, followed by linear part in the low frequency region (See SI-8). The

semicircle corresponds to the charge-transfer resistance at the electrode/electrolyte interface, while the linear relationship in the low frequency region mainly represents pure capacitive behavior. Obviously, the semicircle in the high frequency range of NF/LDH@MnO_2 nanowires is smallest than that of NF/LDH@MnO_2 nanosheets and NF/LDH, indicating a smallest charge-transfer resistance, while the slope of the line for NF/LDH@MnO_2 nanowires is the greatest than that of the other two electrodes, indicating better capacitive behavior and a lower diffusion resistance of ions in the composite. Thus, NF/LDH@MnO_2 nanowires electrode has the lowest lower charge-transfer resistance and ion diffusion resistance than NF/LDH@MnO_2 nanosheets and NF/LDH, resulting in higher reactivity and faster reaction kinetics.

To further evaluate application of the hierarchical NF/LDH@MnO_2 nanowires electrode, we have fabricated an asymmetric supercapacitor and tested it with 1 M LiOH aqueous electrolyte. The asymmetric device exhibits ideal capacitive behavior at potential window up to 2.0 V, which demonstrated good charge-discharge properties and favourable rate capability of the asymmetric supercapacitor (Fig. 6A and 6B). We also test the galvanostatic charge-discharge curves at various current densities (See SI-8), based on which the specific capacitance of the symmetric supercapacitor is calculated to be 75.9 Fg^{-1} at the current density of 1 Ag^{-1}. As the current density increases, the specific capacitance gradually decreases, and 16.8% of the original capacitance can be remained at the density of 10 Ag^{-1}.

Fig. 6C shows Ragone plot of the asymmetric capacitor charged/discharged at different cell voltages. The asymmetric capacitor delivers a low energy density of 8.84 $Whkg^{-1}$ at a power density of 0.7 Wkg^{-1}, which can be attributed to its low specific capacitance and restricted operating voltage (1.4 V). In addition, we also find that energy density of the asymmetric capacitor depends strongly on the cell voltage. In particular, at a cell voltage of 2.0 V, the calculated maximum gravimetric energy density can reach 4.2 $Whkg^{-1}$ (1 Ag^{-1}) and the power densities are 3 and 9 $kWkg^{-1}$ (10 Ag^{-1}), much higher than those of the symmetrical supercapacitors and the LDH- and MnO_2-based asymmetric supercapacitors,[32, 33] which demonstrates the ability of NF/LDH@MnO_2 nanowires as an energy supply component in large-power electrical appliances. As a final test, we connect our prototype device to a red LED and successfully light it (See SI-10). We also evaluate the long-term cycling stability of the asymmetric supercapacitor at a current density of 3 Ag^{-1} for 3000 cycles (Fig. 6D). The device retains 85.3%

of its initial specific capacitance after 3000 cycles, demonstrating a slight damage and disassembly of the electrode materials during the redox reaction. The results highlight the performance of the hierarchical NF/LDH@MnO_2 nanowires electrode, which meets the requirements of both high specific capacitance and excellent cycling stability, two important criteria for practical energy storage devices.

Conclusions

We have successfully prepared hierarchical NF/LDH@MnO_2 nanowire arrays composite through devising a facile and cost-effective strategy. The composite is found to have a large specific capacitance, good rate ability and excellent cycling stability due to the synergistic effect of vertically-aligned and cross-linked LDH nanowalls and ultrathin MnO_2 nanowires. An energy density of 34.2 $Whkg^{-1}$ with a maximum power density of 9 $kWkg^{-1}$ is achieved for the asymmetric supercapacitor device fabricated by using hierarchical NF/LDH@MnO_2 nanowires as a positive electrode and the activated microwave exfoliated graphite oxide activated graphene as a negative electrode. Such binder-free NF/LDH@MnO_2 nanowires electrode shall hold substantial promise for the next generation high-performance supercapacitors.

Acknowledgments

The authors gratefully acknowledge the financial supports provided by National Natural Science Foundation of China (Grant no. 51104194), Doctoral Fund of Ministry of Education of China (20110191120014), National Key laboratory of Fundamental Science of Micro/Nano-device and System Technology (2013MS06, Chongqing University), State Education Ministry and Fundamental Research Funds for the Central Universities (Project no. CDJZR12135501, and CDJZR13130035, Chongqing University, PR China). The authors acknowledge support on electrochemical characterization by Dr. Kexin Yao in King Abdullah University of Science and Technology, Saudi Arabia. Z.W. thanks the financial supports from the National Science Foundation of China under grant no. 11332013, the Grant-in-Aid for Young Scientists (A) (grant no. 24686069), JGC-S Foundation, and Kurata Memorial Hitachi Science and Technology Foundation.

References

1. T. Brezesinski, J. Wang, S. H. Tolbert and B. Dunn, *Nat. Mater.*, 2010, **9**, 146-151.
2. P. Simon and Y. Gogotsi, *Nat. Mater.*, 2008, **7**, 845-854.
3. B. E. Conway, V. Birss and J. Wojtowicz, *J. Power Sources*, 1997, **66**, 1-14.
4. Y. Zhang, H. Feng, X. Wu, L. Wang, A. Zhang, T. Xia, H. Dong, X. Li and L. Zhang, *Int. J. Hydrogen Energy*, 2009, **34**, 4889-4899.
5. H. Wang, H. S. Casalongue, Y. Liang and H. Dai, *J. Am. Chem. Soc.*, 2010, **132**, 7472-7477.
6. H. Zheng, F. Tang, Y. Jia, L. Wang, Y. Chen, M. Lim, L. Zhang and G. Lu, *Carbon*, 2009, **47**, 1534-1542.
7. D. W. Wang, F. Li, J. Zhao, W. Ren, Z. G. Chen, J. Tan, Z. S. Wu, I. Gentle, G. Q. Lu and H. M. Cheng, *ACS Nano*, 2009, **3**, 1745-1752.
8. Y. X. Zhang, F. Li, M. Huang, Y. Xing, X. Gao, B. Li, Z. Y. Guo and Y. M. Guan, *Mater. Lett.*, 2014, **120**, 263-266.
9. M. Huang, Y. Zhang, F. Li, L. Zhang, Z. Wen and Q. Liu, *J. Power Sources*, 2014, **252**, 98-106.
10. Y. X. Zhang, M. Kuang and J. J. Wang, *CrystEngComm*, 2014, **16**, 492-498.
11. K. Chen, Y. Dong Noh, K. Li, S. Komarneni and D. Xue, *J. Phys. Chem. C*, 2013, **117**, 10770-10779.
12. Y. Zhang, C. Sun, P. Lu, K. Li, S. Song and D. Xue, *CrystEngComm*, 2012, **14**, 5892-5897.
13. M. Huang, Y. Zhang, F. Li, Z. Wang, Alamusi, N. Hu, Z. Wen and Q. Liu, *Sci. Rep.*, 2014, **4**, 4518.
14. Y. X. Zhang, M. Huang, F. Li, X. L. Wang and Z. Q. Wen, *J. Power Sources*, 2014, **246**, 449-456.
15. M. Huang, Y. Zhang, F. Li, L. Zhang, R. S. Ruoff, Z. Wen and Q. Liu, *Sci. Rep.*, 2014, **4**, 3878.
16. X. Lang, A. Hirata, T. Fujita and M. Chen, *Nat. Nanotechnol.*, 2011, **6**, 232-236.
17. D. Bélanger, L. Brousse and J. W. Long, *Electrochem. Soc. Interface*, 2008, **17**, 49-52.
18. J. Zhao, Z. Lu, M. Shao, D. Yan, M. Wei, D. G. Evans and X. Duan, *RSC Adv.*, 2013, **3**, 1045-1049.
19. K. H. Chang, Y. F. Lee, C. C. Hu, C. I. Chang, C. L. Liu and Y. L. Yang, *Chem. Comm.*, 2010, **46**, 7957-7959.
20. H. Zhang, X. Yu and P. V. Braun, *Nat. Nanotechnol.*, 2011, **6**, 277-281.
21. J. W. Long, B. Dunn, D. R. Rolison and H. S. White, *Chem. Rev.*, 2004, **104**, 4463-4492.
22. L. Deng, G. Zhu, J. Wang, L. Kang, Z. H. Liu, Z. Yang and Z. Wang, *J. Power Sources*, 2011, **196**, 10782-10787.
23. J. P. Cheng, J. H. Fang, M. Li, W. F. Zhang, F. Liu and X. B. Zhang, *Electrochim. Acta*, 2013, **114**, 68-75.
24. Y. X. Zhang, X. D. Hao, F. Li, Z. P. Diao, Z. Y. Guo and J. Li, *Ind. Eng. Chem. Res.*, 2014, **53**, 6966-6977.
25. Y. Chen, B. Qu, L. Hu, Z. Xu, Q. Li and T. Wang, *Nanoscale*, 2013, **5**, 9812.
26. S. Huang, G. N. Zhu, C. Zhang, W. W. Tjiu, Y. Y. Xia and T. Liu, *ACS Appl. Mater. Interfaces*, 2012, **4**, 2242-2249.
27. J. Fang, M. Li, Q. Li, W. Zhang, Q. Shou, F. Liu, X. Zhang and J. Cheng, *Electrochim. Acta*, 2012, **85**, 248-255.
28. R. R. Salunkhe, K. Jang, S. Lee and H. Ahn, *RSC Adv.*, 2012, **2**, 3190-3193.
29. X. Lu, T. Zhai, X. Zhang, Y. Shen, L. Yuan, B. Hu, L. Gong, J. Chen, Y. Gao and J. Zhou, *Adv. Mater.*, 2012, **24**, 938-944.
30. Z. P. Diao, Y. X. Zhang, X. D. Hao and Z. Q. Wen, *Ceram. Int.*, 2014, **40**, 2115-2120.
31. Z. Wang, X. Zhang, J. Wang, L. Zou, Z. Liu and Z. Hao, *J. Colloid Interface Sci.*, 2013, **396**, 251-257.
32. Y. He, W. Chen, X. Li, Z. Zhang, J. Fu, C. Zhao and E. Xie, *ACS Nano*, 2012, **7**, 174-182.
33. X. Wang, A. Sumboja, M. Lin, J. Yan and P. S. Lee, *Nanoscale*, 2012, **4**, 7266-7272.

List of Figures

Fig. 1. (A) XRD patterns of NF/LDH, NF/LDH@MnO_2 nanowires and NF/LDH@MnO_2 nanosheets; (B) The magnified patterns in the range of 5-25^o for these three samples.

Fig. 2. (A) Schematic illustration of the two-step synthesis of hierarchical NF/LDH@MnO_2 nanocomposites; (B, C) SEM images of NF/LDH@MnO_2 nanowires after immersed the nickel foam in 0.1 M $KMnO_4$ solution at 30 ^{o}C for 4 h; (D, E) SEM images of NF/LDH@MnO_2 nanosheets after the hydrothermal reaction at 140^{o}C for 24 h.

Fig. 3. TEM and HRTEM images of LDH@MnO_2 nanowires (A, B) and LDH@MnO_2 nanosheets. The insets in (A, E) and (B, D) are the corresponding SAED and FFT patterns of LDH@MnO_2 nanowires and LDH@MnO_2 nanosheets, respectively.

Fig. 4. (A, B) Cyclic voltammograms and Galvanostatic discharge curves of hierarchical NF/LDH@MnO_2 nanowires in 1 M LiOH aqueous electrolyte. (C) Cycling performance of the electrode at the current density of 15 A g^{-1}. (D) Specific capacitance and coulombic efficiency of the electrode measured at different current densities.

Fig. 5. (A, B) Cyclic voltammograms and Galvanostatic discharge curves of as-prepared NF/LDH, NF/LDH@MnO_2 nanowires and NF/LDH@MnO_2 nanosheets, recorded at a scan rate of 20 m V s^{-1} and 1 A g^{-1}, respectively. (C) A comparison of specific capacitances for NF/LDH, NF/LDH@MnO_2 nanowires and NF/LDH@MnO_2 nanosheets electrode at different current density. (D) Cycling performance of these three electrodes at the current density of 10 A g^{-1}. The mass of the active materials for NF/LDH, NF/LDH@MnO_2 nanowires and NF/LDH@MnO_2 nanosheets are 1.34, 1.67, 1.8 mg, respectively.

Fig. 6. (A) CV curves of NF/LDH@MnO_2 nanowires symmetric supercapacitor measured at different potential window at a scan rate of 50 mV s^{-1}. (B) CV curves of the symmetric supercapacitor measured at different scan rates between 0 and 1.8 V. (C) Ragone plot of energy density and power density of symmetric devices based on NF/LDH@MnO_2 nanowires electrode. (D) Cycling performance of the symmetric supercapacitor at the current density of 3 A g^{-1}.

Fig. 1

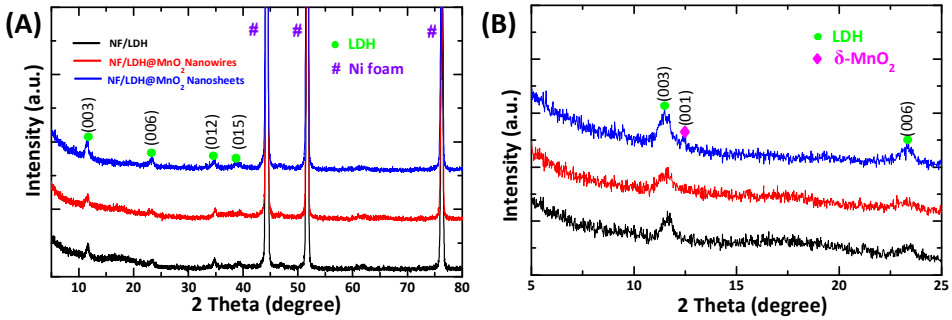

Fig. 2

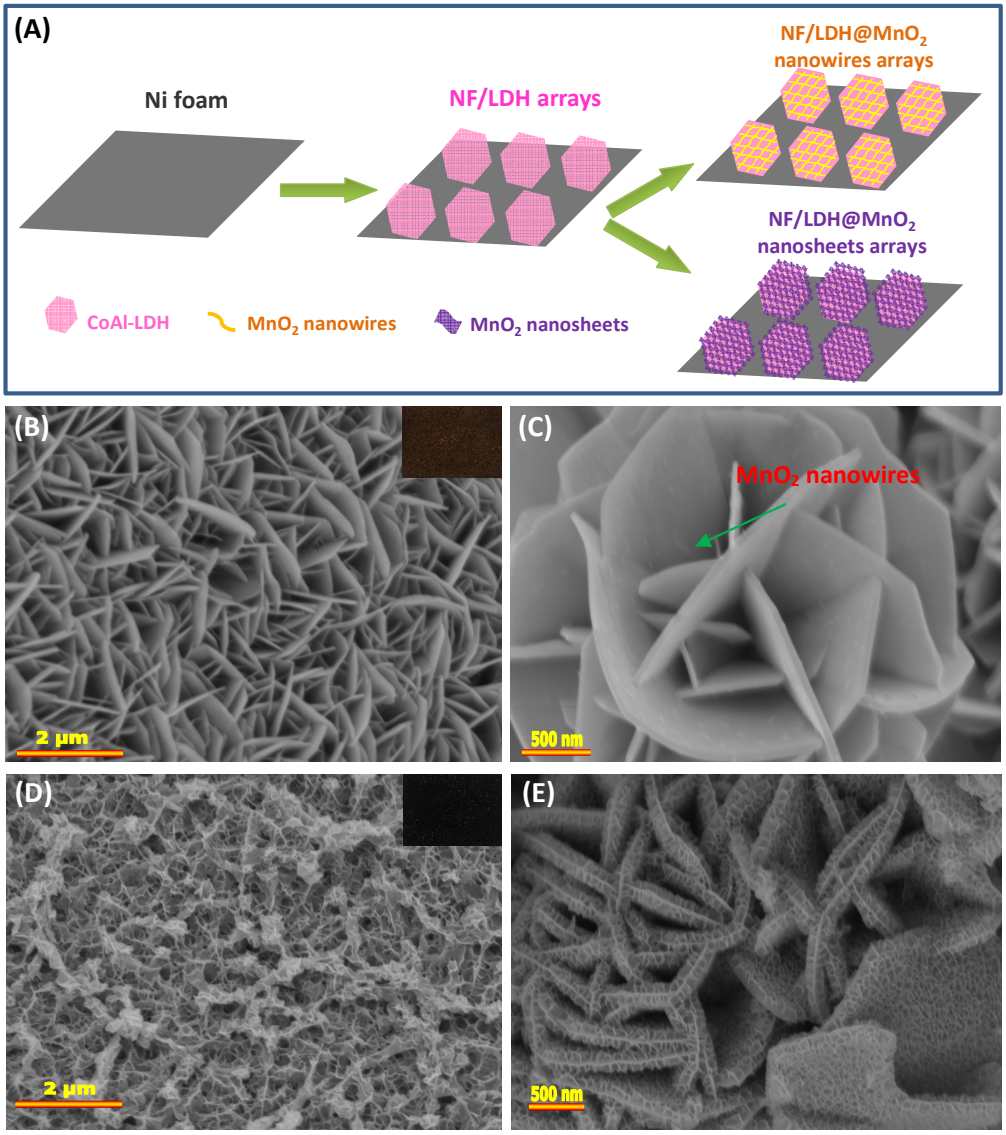

Fig. 3

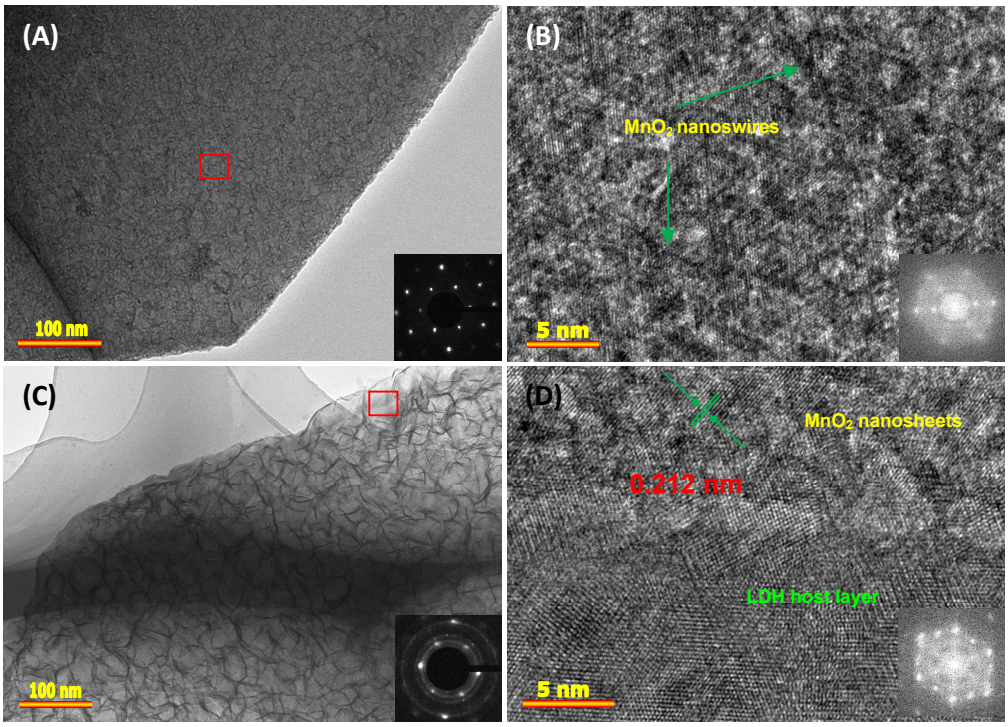

Fig. 4

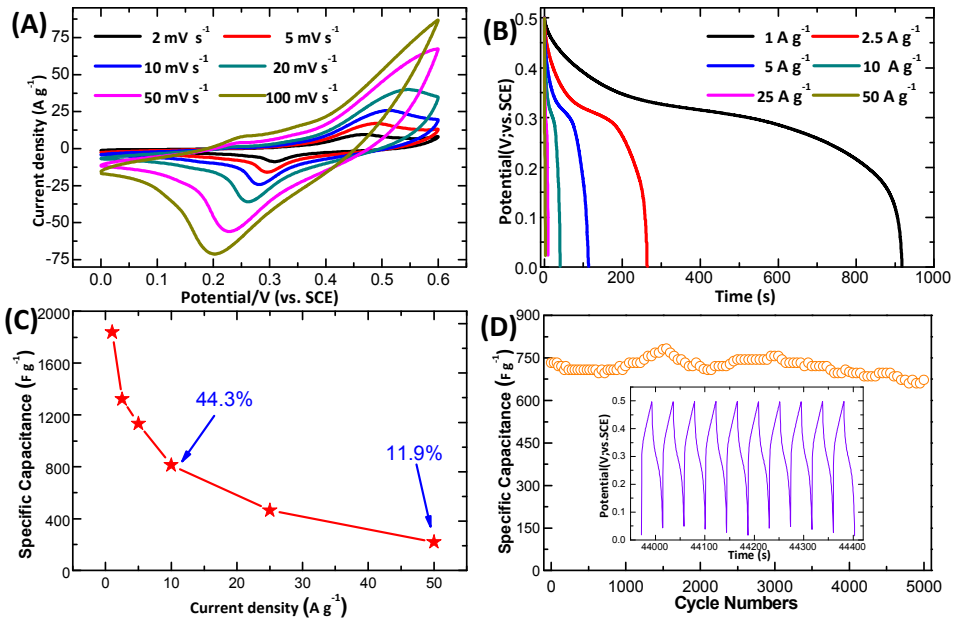

Fig. 5

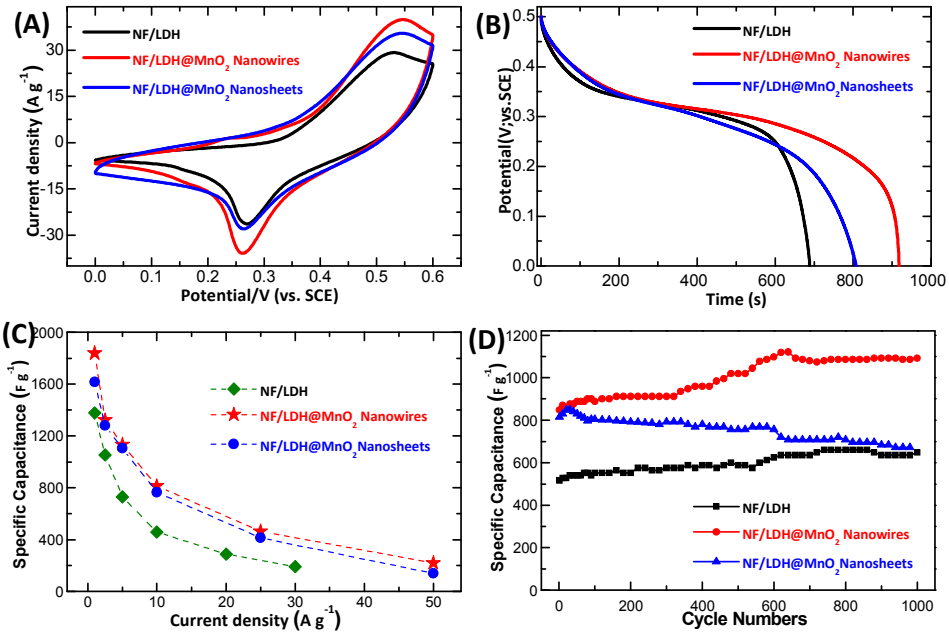

Fig. 6